Dislocation Descriptors of Low and High Angle Grain Boundaries with Convolutional Neural Networks

William Noh, Huck Beng Chew*

Department of Aerospace Engineering, University of Illinois at Urbana-Champaign, Urbana IL 61801, USA

*Author to whom all correspondence should be addressed. Email: hbchew@illinois.edu

Abstract

Multiscale modeling of plasticity in polycrystalline metals is a long-standing challenge in part because of the lack of an accepted grain boundary descriptor, which has hindered the bridging of scales between atomistic simulations and meso-scale discrete dislocation dynamics (DDD) models. While grain boundary dislocations (GBDs) for low angle grain boundaries can be ascertained by Burgers circuit analyses, the dislocation structures of high angle grain boundaries have remained elusive because of overlapping dislocation core fields. Here, we use convolutional neural networks (CNNs) to establish the locations of GBDs responsible for the misorientations of <001> symmetrical-tilt Cu grain boundaries, from the local atomistic stress fields modeled with molecular dynamics (MD) simulations. We achieve accurate CNN predictions of GBDs with sub-angstrom resolution across an extensive set of low- to high-tilt-angle grain boundaries through a training dataset, generated from superposing continuum-representations of the MD stress fields of single dislocations that consider the contributions of both the Volterra and dislocation core fields. The approach paves the way for dislocation representations of the atomistic grain boundary structures modeled by MD simulations or density functional theory (DFT) calculations in mesoscale DDD models to elucidate multiscale plasticity effects.

Keywords: Grain boundary dislocation; dislocation core; atomistic stress; machine learning; molecular dynamics

1. Introduction

Grain boundaries of polycrystalline metals are among the most well studied but least understood material interfaces. It is now well accepted that plasticity at the macroscale originates from the motion and interaction of dislocations across grains through atomistic mechanisms, such as dislocation absorption, transmission, emission or pile-up at the grain boundaries [1-3]. Each of these mechanisms is highly sensitive to the atomistic structure of the grain boundary, and the structure of the boundary is in turn altered by the ensuing dislocation-grain boundary interactions [4-10]. Molecular dynamics (MD) simulations can capture this continuously evolving atomistic structure of the grain boundary, but upscaling these simulations to the meso-scale through discrete dislocation dynamics (DDD) models poses a significant challenge since treatment of the dislocation-grain boundary interactions often rely on a predefined set of phenomenological rules [11-16].

Studies show that the evolving atomistic structure of the grain boundary with dislocation emission, absorption or transmission can be attributed to its evolving dislocation content [17-19]. This supports the early notion that the tilt and twist misorientation between two crystalline lattices are fundamentally created by arrays of intrinsic grain boundary dislocations (GBDs) adjoining the boundary [20,21]. Such dislocation-based grain boundary descriptors, however, are problematic for higher angle grain boundaries. While the atomistic structures of low angle grain boundaries are reasonably well-defined by their linear elastic displacement fields, the close proximity between GBDs in higher angle grain boundaries result in overlapping cores, which clouds the relationship between the linear elastic fields and the dislocation structure of the boundary [19]. In addition,

resolution of the net or resultant Burgers vector about these high angle grain boundaries into Burgers vectors of discrete dislocations is not unique, since one could potentially achieve the same misorientation angle with alternative sets of GBDs [20,21]. Because of these issues, later studies have described the grain boundary as a combination of building blocks or structural units (SUs), with each SU representing particular arrangements of a limited number of atoms [22-26]. Fundamental properties of the boundary have been linked to the presence of certain SUs – for example, the propensity to emit Shockley partials under tension and compression has been attributed to the presence of E- and A-type SUs, respectively, along symmetrical-tilt <110> grain boundaries [27,28]. More recently, studies have established the local atomistic stress state along a grain boundary as a representation of the Cauchy stress tensor for the calculation of continuum traction fields, which ultimately governs the ability of grain boundaries to emit, absorb, or transmit dislocations [28-30]. Nevertheless, tracking the continuously evolving SUs or traction signatures along each boundary poses a challenge in DDD simulations. In contrast, a dislocation-based descriptor provides a representation of the grain boundary in terms of fundamental entities (i.e., dislocations) already explicitly modeled in DDD simulations.

In the presence of a dislocation, the distortion resulting from displacement of atoms in a crystal from their perfect lattice sites produces an elastic Volterra stress field outside the core of the dislocation [31,32]. Within a radius of ~10 to 50 burgers vector, Å, from the dislocation line, nonlinear dislocation core configurations give rise to an additional linear elastic dislocation core field, which is superposed onto the Volterra field [33,34]. Although the core-field is shorter range than the Volterra field, it significantly influences the forces between dislocations at close range, such as during dislocation pile-up, and is conceivably the dominant component in high angle grain boundaries with closely-spaced GBDs. By extension, a GBD therefore acts as a source of internal

stress along the grain boundary, with its stress signature arising from its core and Volterra fields. The combined interaction of an array of GBDs constituting a grain boundary is ultimately responsible for the internal stress field ($\bar{A}_{\bar{A}}$) near a grain boundary [28-30].

Elucidating the dislocation structure of a grain boundary from its atomistic stress field is a non-trivial inverse problem, particularly in the presence of overlapping dislocation core fields. Recent studies in machine learning show that deep neural network architectures are capable of solving a wide variety of inverse problems. For example, neural networks have been used to predict phase diagrams and phase transitions [35], grain boundary energy [36], grain boundary segregations [37], grain boundary damage [38], atomistic stresses [39], deformation constitutive behavior of materials [40-44], as well as the potential energy and atomic force of metals modeled in density functional theory (DFT) [45]. Here, we adopt a convolutional neural network (CNN) for machine learning to detect the presence, and predict the locations, of GBDs (output) from atomistic stress information (input) across an extensive range of low to high angle <001> symmetrical-tilt grain boundaries. Section 2 details the modeling of the grain boundaries with MD simulations. Section 3 describes the CNN architecture, along with the training datasets of the neural network generated from the superposition of single (isolated) dislocation stress fields. We present results for our neural network predictions of GBDs in Section 4, and introduce a continuum representation of the stress fields of discrete dislocations to improve training of our neural network for high-tilt-angle boundaries. In Section 5, we discuss the implications of our neural network in obtaining dislocation representations of grain boundaries, especially in the bridging of scales between atomistic (MD, DFT) simulations and DDD models at the meso-scale. Section 6 concludes with a summary.

2. Grain Boundary Modeling

While edge dislocations tend to dissociate to form partial dislocations along <110> grain boundaries [28], dislocations along <001> grain boundaries retain their distinctive edge character and have Burgers vector perpendicular to the plane of the grain boundary. We create a series of <001> symmetrical-tilt Cu grain boundary model structures using the classical MD simulator LAMMPS [46], where the Embedded Atom Method (EAM) potential governs the interatomic interactions between Cu atoms [47]. This potential closely reproduces the bulk lattice (3.615 Å) and elastic constants ($C_{11} = 167$ GPa, $C_{12} = 124$ GPa, $C_{44} = 76$ GPa) of Cu, which are comparable to experimental measurements and tight-binding calculations [48-50]. We create each bicrystal model structure by first rotating two perfect face-centered-cubic (FCC) Cu single crystals by a tilt angle $\pm\frac{\bar{A}}{2}$ about the [001] direction ($\bar{A}_3$-axis), with the grain boundary located along the $\bar{A}_1$-axis. We displace the top crystal laterally with respect to the bottom crystal in 1% increments of the unit structural length of the grain boundary along the $\bar{A}_1$ direction, and remove any overlapping atoms. This process is iteratively repeated to generate a multiplicity of possible metastable grain boundary states with the same $\bar{A}$.

Each resulting grain boundary configuration is subjected to energy minimization in MD, and the model configuration with the lowest energy is selected as the representative Cu grain boundary structure with that particular tilt angle. A total of 18 minimum energy grain boundary structures are generated through this process, with tilt angles varying from $\bar{A} = 3.28°$ to $53.13°$, to cover the spectrum of low- ($\bar{A} \leq 14.25°$), moderate- ($16.26° \leq \bar{A} \leq 22.62°$), and high-tilt-angle ($\bar{A} \geq 28.06°$) grain boundaries (Fig. 1). Additionally, a grain boundary structure with a very low tilt angle of $\bar{A} = 0.818°$ is also created, and is considered as an "isolated" edge dislocation structure – the periodic spacing between these "isolated" edge dislocations is ~25 nm, which is sufficiently

far for the MD stress fields of these periodic dislocation images (constructed from virial theorem) to be treated as non-interacting (see Fig. S1 of the Supplementary Materials).

3. Convolution Neural Network

The dislocation content of a grain boundary with tilt rotation $\bar{A}$ can be quantified by the classical Frank-Bilby equation [51],

$$\bar{A}_{\bar{A}} = \bar{A}/\left(2\sin\frac{\bar{A}}{2}\right) \quad (1)$$

where $\bar{A}_{\bar{A}}$ is the mean separation between dislocations in the boundary, and $\bar{A}$ is the magnitude of a Burgers vector of a perfect dislocation in the crystal. This equation suggests that the tilt angle of each grain boundary must be partitioned among several sets of parallel edge dislocations. In atomistic simulations and microscopy experiments, one can perform a Burgers circuit analysis (black circles in Fig. 1b-top) to confirm the Burgers vector and hence the presence of individual GBDs. By constructing multiple non-overlapping Burgers circuits, and identifying those that contain a dislocation, one can further pinpoint the location of individual GBDs with atomic precision. Analysis tools based on this approach, such as the dislocation extraction algorithm (DXA) and the on-the-fly dislocation detection algorithm (ODDA), are able to quantify the approximate dislocation locations from atomic position information [52,53]. We include the DXA-predicted GBD locations along our low- to moderate-tilt-angle grain boundaries in Fig. 1a,b. Predictions from the Burgers circuit analysis, however, fall short for high angle grain boundaries (e.g. Fig. 1c) – the GBDs are no longer distinct defects due to overlapping dislocation cores and the absence of perfect FCC crystal lattice separating the disordered regimes. Nevertheless, since the GBDs are fundamental elements of a grain boundary structure that create the tilt (and twist) misorientation between two crystalline lattices adjoining the boundary, the observed atomistic

grain boundary field stresses and associated grain boundary tractions [28,29] should originate from these intrinsic GBDs. Here, we detail the training, validation and testing of a convolutional neural network (CNN) to establish the dislocation structures of low- to high-tilt-angle grain boundaries (output) from the grain boundary field stresses (input).

3.1 Neural network architecture

The nonlinear stress fields ($\bar{A}_{11}$, $\bar{A}_{12}$, $\bar{A}_{22}$) near the grain boundaries are fed to a CNN to detect the presence of a GBD within the input images and to predict its ($\bar{A}_1, \bar{A}_2$) location. In between the input and output layers are the hidden layers starting with a convolutional tool made up of many repeated convolution, ReLU activation, and max pooling layers for feature extraction, as depicted in Fig. 2. Similar to previously employed CNNs for image classification [54], each convolution layer is a filter represented by a matrix of weights, which convolves over the mappings in the previous layer. The ReLU activation layer after each convolution enables the CNN to learn complex functions more efficiently by introducing nonlinearities to the numerical mappings, while the maxpool layers reduce the spatial dimensions of the mappings by selecting the maximum values and provide the translation invariance characteristic of the CNN. In the final layer of the convolutional tool, we forgo the maxpool layer because of the limited spatial dimensions of its preceding input, and separately connect the final ReLU activation layer to two parallel and independent fully-connected (FC) layers for dimensionality reduction and feature combination. The first FC layer is subjected to a softmax activation function, which provides a probabilistic interpretation of output values through a 2×1 vector with probabilities denoting the presence ($\bar{A}_0$) and absence ($\bar{A}_1$) of a dislocation ($\bar{A}_0 + \bar{A}_1 = 1$). The second FC layer outputs a 2×1 vector representing the ($\bar{A}_1, \bar{A}_2$) location of the detected GBD; its output is set to a location of (0,0) and ignored in the absence of a dislocation. During training of the CNN, the initially randomized weights of the model are

optimized through backpropagation using the Adam's optimizer to minimize a two-part loss function, comprising of a cross-entropy loss for the classification problem of dislocation detection from the first FC layer, and a smooth L1 loss for the $(\bar{A}_1, \bar{A}_2)$ dislocation location prediction from the second FC layer, with equal weights assigned to the respective loss components.

3.2 Training dataset generation

Our input-output training dataset for the CNN is generated by superposing the stress field of individual edge dislocations with random spatial arrangements along the $\bar{A}_1$-axis (Fig. 3-top) to create multiple instantiations of possible "grain boundary" stress fields (Fig. 3-bottom). The analytical expression for the linear elastic Volterra stress field of isolated edge dislocations is commonly used to describe dislocation interactions in DDD simulations [31,32]. Aside from the Volterra field, however, dislocations possess a core field, which can be significant up to a distance of ten Burgers vector from the dislocation line [33]. We note that the periodic spacing between GBDs, $\bar{A}_{\bar{A}}$, falls below twice this distance even for very low angle grain boundaries (Table 1), suggesting the importance of core field effects. We further illustrate this by comparing the stress distributions associated with the Volterra field versus MD field (which incorporates core effects) of an isolated edge dislocation, centered along the $\bar{A}_3$-axis, in Figs. S1 and S2 of the Supplementary Materials. We observe that the stress contours are generally well-described by the Volterra field after a certain distance from the dislocation line, but the stress distributions are very different within the core region.

Prior studies have represented the contribution of core effects using linear anisotropic elasticity theory with force and dislocation dipoles; this contribution is superposed on the Volterra field to describe the overall dislocation field stresses and strains [33,34]. Here, we directly account for both the core and Volterra fields using the MD stress field of an isolated edge dislocation

computed from Virial theorem (Fig. S1b of the Supplementary Materials), with Voronoi tessellation cells over each atom. We subdivide this Voronoi stress field into 0.5×0.5 Å^2 pixels, and average the $\bar{A}_{\bar{A}\bar{A}}$ stresses within each pixel. For each 200×200 Å^2 simulated "grain boundary" structure represented by random spatial distributions of edge dislocations along the $\bar{A}_1$-axis (Fig. 3-top), we superpose the pixelated stresses centered about each edge dislocation to obtain the "grain boundary" stress field (Fig. 3-bottom). We train our CNN to predict the presence of a dislocation, and its subsequent location, if its center core lies within a 20×20 pixel^2 (10×10 Å^2) sample representing a detection window (Fig. 3-bottom). We also ensure that no more than one dislocation is present within each detection window in our training dataset. We remark that the pixel size selected has to be sufficiently small to capture the features of the object (GBD) being detected, since too large of a pixel would average out the heterogeneous stress distributions and cause issues with localization of the GBDs. However, too small of a pixel would significantly increase the computational expense to train the CNN. Our heuristic choice of a pixel size of 0.5×0.5Å^2, which is several-folds smaller than the Voronoi cell area, allows the large stress field variations within the core of each GBD to be adequately captured. The localization predictions are expected to have an intrinsic uncertainty of ~0.5Å.

3.3 Hyperparameter testing

We generate 9,000 samples, with an equal split between samples with and without dislocations to ensure a balanced dataset. We subdivide 60%, 20%, and 20% of these samples into training, validation, and testing datasets, respectively. To optimize the CNN architecture, we perform hyperparameter testing by systematically varying the learning rate, number of convolutional layers, and the type of activation layers; we also perform a limited study on the effects of the max pooling layer by changing the default kernel (size 2×2 and stride 2) only for the third convolution

layer (if applicable). We quantify the CNN performance based on its ability to (a) correctly detect the presence or absence of dislocations within the sampling image (detection accuracy), as well as (b) predict the dislocation location within a 4×4 pixel^2 (2×2 Å^2) square grid from its core center for samples containing dislocations (localization accuracy). We train each model on the training dataset for 100 epochs and we select the epoch with the lowest validation loss from the validation dataset. We further confirm that this validation loss is similar to the loss from the testing dataset at the 100 epoch, which suggests generalizability of the CNN to unseen data. Results of the hyperparameter study are summarized in Table S1 of the Supplementary Materials. Our studies show that the learning rate is the most critical hyperparameter (optimal at 1e-5), followed by the number of convolutional layers (≥ 3 layers are necessary). Our final CNN architecture has a learning rate of 1e-5, with 4 convolutional layers, each coupled to a ReLU activation layer, followed by a max pooling kernel of size 2×2 and stride 2, except for the final convolutional layer where the activation layer is separately coupled to two parallel FC layers. Because of the low computational cost of training the neural network (longest runtime to train a CNN for 100 epochs with a batch size of one is 170.18 minutes on a 3.70 GHz Intel i9-10900X processor with 10 cores) and the near-perfect predictive accuracies already achieved with this neural network architecture, we did not further optimize the remaining hyperparameters, such as the type of optimizer, training step size, and accuracy variance in the training cycle.

4. Results

4.1 Low to moderate angle grain boundaries

Our CNN architectures in Section 3.3 are trained on datasets generated by randomly positioning edge dislocations along the $\bar{A}_1$-axis (generally, $\bar{A}_1 \neq \bar{A}_2 \neq \bar{A}_3$ ... ... in Fig. 3-top), and superposing the discrete (pixelated) MD stress fields for isolated edge dislocations (Fig. 3-bottom).

Recognizing that the <001> symmetrical-tilt Cu grain boundary structures of interest comprise of only periodic arrays of GBDs with fixed periodicity $\bar{A}_{\bar{A}}$, we repeat the training process outlined in Section 3.3 to train a new CNN based on periodically-distributed edge dislocations along the $\bar{A}_1$-axis – each training data has random but equal GBD spacings ($\bar{A}_1 = \bar{A}_2 = \bar{A}_3$ ... ... in Fig. 3-top). We find that this new CNN, trained on the periodic dataset, outperforms the previous CNN trained on the non-periodic dataset (Section 3.3). We then elucidate the ability of this newly-trained CNN to accurately detect and quantify the dislocation structures of <001> symmetrical-tilt grain boundaries of varying tilt angles, based on the MD-computed grain boundary stresses as the input to the CNN.

We first focus on low- to moderate-tilt-angle grain boundaries of $\bar{A} = 3.28°$ to $22.62°$ where the location of GBDs can still be ascertained by DXA analysis. However, the resolution of DXA analysis is limited to the size of the smallest possible Burgers circuit that can be constructed; a more accurate assessment of the ground truth location for these GBDs can be estimated from the inflection point between the maximum tensile and compressive $\bar{A}_{11}$ and $\bar{A}_{22}$ stresses along $\bar{A}_2 = 0$ (Figs. S1 and S2 of the Supplementary Materials). Based on this "ground truth" representation of the GBD locations, we quantify the true positive and true negative dislocation detection accuracies by sliding a 10×10 Å^2 detection window in single pixel (0.5×0.5 Å^2) increments along the $\bar{A}_1$- and $\bar{A}_2$-axis of each grain boundary structure. For samples where a dislocation is present within the detection window, we also compute the localization error as the average difference between the predicted dislocation location and its "actual" ground truth location. As summarized in Table 1, our CNN trained on the discrete (pixelated) superposed stress field of dislocation arrays is able to detect with 100% accuracy the presence of an edge dislocation across these grain boundary structures, albeit with an observable false positive prediction (~15%). The localization predictions

are surprisingly accurate, with mean location predictions residing well within a single 0.5×0.5 Å^2 pixel from the ground truth location, which is the current limit of our localization resolution.

We show in Fig. 4 a sampling of detection windows for grain boundaries with varying tilt angles where true positive (colored boxes) dislocations are detected, along with the predicted locations (corresponding colored dislocation symbols) of these detections. We remark that the false positive detections are consistently associated with sampling windows just outside the ± 1 Å error bound (solid black box) centered at the core of the GBD (black cross). Interestingly, the localization predictions are very accurate, providing a mean GBD location (green dislocation symbol) that almost overlaps with the actual ground truth predictions, even at moderate grain boundary tilt angles of $\bar{A} = 16.26°$ and 22.62° (Fig. 4c and 4d). This high accuracy can be attributed to the generally similar grain boundary stress fields from MD simulations versus the reconstructed stress fields from superposing the pixelated MD stress fields of isolated edge dislocations, as shown in Fig. 5, since the superposed fields are used for the training of our CNN. We observe minor variations in the localization predictions (green dislocation symbols) among neighboring GBDs along each of the symmetrical-tilt grain boundaries, which we attribute to small translation of pixels because the grain boundaries modeled in MD do not have periodicities that are exactly divisible by the pixel dimension of 0.5Å. Close examination also shows that the dislocation cores of these superposed fields are slightly more diffused compared to the actual MD grain boundaries, and have a distinct neutral zone within its compressive core. Our MD simulations show that this neutral zone dissipates for tilt angles of $\bar{A} = 5.45°$ and beyond, suggesting some structural changes to the core even at these low tilt angles. The presence of this neutral zone, however, has little apparent bearing on the CNN's ability to detect and localize the GBDs.

4.2 High angle grain boundaries

DXA analysis cannot identify the dislocation structures of high angle grain boundaries beyond $\bar{A} > 22.62°$, since the cores of the closely-spaced GBDs are now overlapping. In contrast, our trained CNN is able to detect the presence of GBDs in both the $\bar{A} = 28.06°$ and 36.85° grain boundaries with very high accuracy, as shown in Table 1. While the exact GBD location can be ascertained with high confidence for the $\bar{A} = 28.06°$ grain boundary, poor localization predictions are obtained for the $\bar{A} = 36.85°$ grain boundary. Figure 6a and 6b shows the sampling of true positive detection windows (colored boxes) for both these high-tilt-angle grain boundaries, along with the corresponding locations of these detected dislocations (colored dislocation symbols). For the $\bar{A} = 28.06°$ grain boundary, there is surprisingly very limited spread in the predicted GBD locations, suggesting high accuracy of the CNN even when the cores are overlapping. In contrast, we observe a huge scatter in dislocation location predictions for the $\bar{A} = 36.86°$ grain boundary with average predictions (green dislocation symbol) falling well outside of the ± 1 Å error bound (solid black box) centered at the core of the GBD, which suggests a lack of confidence in the CNN predictions.

To elucidate the contrasting performance of the CNN towards both these high-tilt-angle boundaries, we compare the reconstructed stress fields of these boundaries from superposition of the periodic GBDs versus the actual MD stress fields (Fig. 6c and 6d). Unlike low- to moderate-tilt-angle grain boundaries, distinct differences are now observed between the superposed and actual MD grain boundary fields for both these high-tilt-angle grain boundaries. For the $\bar{A} = 28.06°$ grain boundary, there is still good general agreement between the superposed and actual MD stress fields within the core of the GBDs, which allows the neural network to correctly localize the GBDs, but the reconstructed field increasingly deviates from the actual MD stress field with radial distance from the center cores of these GBDs. For the $\bar{A} = 36.86°$ grain boundary, there is

now complete lack of correlation between the superposed stress field used in the training dataset of the CNN and the actual MD grain boundary field, which explains the poor predictive localization performance of the CNN. We attribute the discrepancies between the superposed and MD fields to: (a) changes to the dislocation core structure with increasing proximity/overlap of the GBDs, and (b) numerical errors associated with superposition of the discrete stress fields for isolated edge dislocations used for the training of the CNN. The former could warrant incorporating the MD fields of closely-spaced but clearly identifiable dislocation structures within the training dataset, and is discussed in Section 5. The latter contributes to an accumulation of error with increasing density of superposed GBDs, and hence is exacerbated for high-tilt-angle grain boundaries with shorter grain boundary period, $\bar{A}_{\bar{A}}$.

One distinct characteristic of GBDs is the clear demarcation between tension and compression zones. We theorize that the distinct patterns associated with positive and negative contours of individual $\bar{A}_{\bar{A}\bar{A}}$ stress components near the grain boundary is, to a first order, the key feature that enables the neural network to pinpoint the exact location of GBDs. Accordingly, we delineate the grain boundary stress field into tension ($\bar{A}_{\bar{A}\bar{A}} > 1$ GPa), neutral ($\left|\bar{A}_{\bar{A}\bar{A}}\right| \leq 1$ GPa), and compression ($\bar{A}_{\bar{A}\bar{A}} < -1$ GPa) zones. For grain boundaries with low- and moderate-tilt-angles in Fig. 7, we can clearly identify unique stress signatures associated with individual GBDs along the boundary which are exhibited by both the MD and superposed fields. For the high-tilt-angle grain boundary with $\bar{A} = 28.06°$ in Fig. 8, distinctive tension, neutral and compression zones are still exhibited by both the MD and superposed $\bar{A}_{\bar{A}\bar{A}}$ field, though some background noise is now observed for the latter. This background noise permeates the entire superposed stress field for the $\bar{A} = 36.86°$ grain boundary, which clouds the compression-tension stress patterns and the ability of a CNN to identify the GBD signatures for these high-tilt-angle boundaries.

4.3 Continuum field representation of dislocations

To increase the accuracy of our superposed stress fields in our training dataset for the CNN, we introduce a spectral (field projection) method [28-30] to obtain a continuum-representation of the stress-field ($\bar{A}_{\bar{A}\bar{A}}^{\bar{A}}$) of a single isolated edge dislocation from the discrete atomistic stress field modeled in MD ($\bar{A}_{\bar{A}\bar{A}}^{\bar{A}\bar{A}\bar{A}}$). The 2D continuum stress field can be represented by a Fourier series,

$$\bar{A}_{\bar{A}\bar{A}}^{\bar{A}} = \sum_{\bar{A}=0}^{\bar{A}} \sum_{\bar{A}=0}^{\bar{A}} \bar{A}_{\bar{A}\bar{A}}^{\bar{A}\bar{A}} \sin\left(\frac{\bar{A}\bar{A}\bar{A}_1}{\bar{A}}\right) \sin\left(\frac{\bar{A}\,\bar{A}\bar{A}_2}{\bar{A}}\right) + \bar{A}_{\bar{A}\bar{A}}^{\bar{A}\bar{A}} \sin\left(\frac{\bar{A}\bar{A}\bar{A}_1}{\bar{A}}\right) \cos\left(\frac{\bar{A}\,\bar{A}\bar{A}_2}{\bar{A}}\right) +$$

$$\bar{A}_{\bar{A}\bar{A}}^{\bar{A}\bar{A}} \cos\left(\frac{\bar{A}\bar{A}\bar{A}_1}{\bar{A}}\right) \sin\left(\frac{\bar{A}\,\bar{A}\bar{A}_2}{\bar{A}}\right) + \bar{A}_{\bar{A}\bar{A}}^{\bar{A}\bar{A}} \cos\left(\frac{\bar{A}\bar{A}\bar{A}_1}{\bar{A}}\right) \cos\left(\frac{\bar{A}\,\bar{A}\bar{A}_2}{\bar{A}}\right) \tag{2}$$

where ($\bar{A}_{\bar{A}\bar{A}}^{\bar{A}\bar{A}}$, $\bar{A}_{\bar{A}\bar{A}}^{\bar{A}\bar{A}}$, $\bar{A}_{\bar{A}\bar{A}}^{\bar{A}\bar{A}}$, $\bar{A}_{\bar{A}\bar{A}}^{\bar{A}\bar{A}}$) are the unknown coefficients to be determined using the orthogonality rule. By approximating $\bar{A}_{\bar{A}\bar{A}}^{\bar{A}} \cong \bar{A}_{\bar{A}\bar{A}}^{\bar{A}\bar{A}\bar{A}}$ when averaged over the periodic domain,

$$\begin{aligned}
\bar{A}_{\bar{A}\bar{A}}^{\bar{A}\bar{A}} &= \frac{1}{\bar{A}^2} \iint_{-\bar{A}}^{\bar{A}} \bar{A}_{\bar{A}\bar{A}}^{\bar{A}\bar{A}\bar{A}} \sin\left(\frac{\bar{A}\bar{A}\bar{A}_1}{\bar{A}}\right) \sin\left(\frac{\bar{A}\,\bar{A}\bar{A}_2}{\bar{A}}\right) \bar{A}\bar{A}_1 \bar{A}\bar{A}_2 \\
\bar{A}_{\bar{A}\bar{A}}^{\bar{A}\bar{A}} &= \frac{1}{\bar{A}^2} \iint_{-\bar{A}}^{\bar{A}} \bar{A}_{\bar{A}\bar{A}}^{\bar{A}\bar{A}\bar{A}} \sin\left(\frac{\bar{A}\bar{A}\bar{A}_1}{\bar{A}}\right) \cos\left(\frac{\bar{A}\,\bar{A}\bar{A}_2}{\bar{A}}\right) \bar{A}\bar{A}_1 \bar{A}\bar{A}_2 \\
\bar{A}_{\bar{A}\bar{A}}^{\bar{A}\bar{A}} &= \frac{1}{\bar{A}^2} \iint_{-\bar{A}}^{\bar{A}} \bar{A}_{\bar{A}\bar{A}}^{\bar{A}\bar{A}\bar{A}} \cos\left(\frac{\bar{A}\bar{A}\bar{A}_1}{\bar{A}}\right) \sin\left(\frac{\bar{A}\,\bar{A}\bar{A}_2}{\bar{A}}\right) \bar{A}\bar{A}_1 \bar{A}\bar{A}_2 \\
\bar{A}_{\bar{A}\bar{A}}^{\bar{A}\bar{A}} &= \frac{1}{\bar{A}^2} \iint_{-\bar{A}}^{\bar{A}} \bar{A}_{\bar{A}\bar{A}}^{\bar{A}\bar{A}\bar{A}} \cos\left(\frac{\bar{A}\bar{A}\bar{A}_1}{\bar{A}}\right) \cos\left(\frac{\bar{A}\,\bar{A}\bar{A}_2}{\bar{A}}\right) \bar{A}\bar{A}_1 \bar{A}\bar{A}_2
\end{aligned} \tag{3}$$

Based on equilibrium conditions, the average normal and shear tractions along each cross-sectional cut parallel to the $\bar{A}_1$- or $\bar{A}_2$-axis should be zero for a single edge dislocation with its core centered about the $\bar{A}_3$-axis – a condition that is clearly not satisfied by our superposed discrete (pixelated) $\bar{A}_{\bar{A}\bar{A}}$ stress fields, particularly for the high-tilt-angle grain boundaries in Fig. 8. In addition, the $\bar{A}_{11}$ field for a single isolated edge dislocation with Burgers vector normal to the $\bar{A}_1$-axis generally has equal magnitude but opposite sign about the $\bar{A}_2$-axis (Figs. S1 and S2 of the Supplementary Materials), except at distances very close to the dislocation core. This lack of strict enforcement of equilibrium and symmetry constraints for the atomistic (virial) stress fields of an isolated

dislocation results in significant accumulation of error once we superpose these discrete fields for the training of the CNN, as shown by the increasing background noise of the superposed fields with grain boundary tilt-angle in Figs. 7 and 8. Here, we set $\bar{A}^{11}_{0\bar{A}} = \bar{A}^{11}_{0\bar{A}} = 0$, $\bar{A}^{22}_{\bar{A}\,0} = \bar{A}^{22}_{\bar{A}\,0} = 0$, and $\bar{A}^{12}_{0\bar{A}} = \bar{A}^{12}_{\bar{A}\,0} = \bar{A}^{12}_{0\bar{A}} = \bar{A}^{12}_{\bar{A}\,0} = 0$ in (2) and (3) to enforce the equilibrium constraints of $\int \bar{A}_{11}\,\bar{A}\bar{A}_2 = 0$, $\int \bar{A}_{22}\,\bar{A}\bar{A}_1 = 0$, and $\int \bar{A}_{12}\,\bar{A}\bar{A}_1 = \int \bar{A}_{12}\,\bar{A}\bar{A}_2 = 0$, respectively. In addition, we enforce the symmetry constraint resulting in $\int \bar{A}_{11}\,\bar{A}\bar{A}_1 \approx 0$ by setting $\bar{A}^{11}_{\bar{A}\,0} = \bar{A}^{11}_{\bar{A}\,0} = 0$ in (2) and (3). We find that the $\bar{A}^{\bar{A}}_{\bar{A}\bar{A}}$ field convergences between $\bar{A} = \bar{A} = \sim$150 to 250 terms, and we select $\bar{A} = \bar{A} = 250$ terms in our Fourier construction of $\bar{A}^{\bar{A}}_{\bar{A}\bar{A}}$. Since $\bar{A}^{\bar{A}}_{\bar{A}\bar{A}}$ is continuous and satisfies the equilibrium equations, we consider (2) to provide a continuum-equivalent representation of the combined core and Volterra field of an isolated edge dislocation.

The periodicity of our Fourier series is defined on the interval $(-\bar{A}, \bar{A})$ along both the $\bar{A}_1$- and $\bar{A}_2$-directions. As such, $\bar{A}$ has to be sufficiently large for $\bar{A}^{\bar{A}\bar{A}}_{\bar{A}\bar{A}}$ to dissipate so that periodic images of the edge dislocation through the Fourier series will not influence the stress field in the $\bar{A}_2$-direction. Along the $\bar{A}_1$-axis, however, we seek to superimpose multiple equally-spaced edge dislocations (representing the periodic grain boundary spacing $\bar{A}_{\bar{A}}$) to generate training sets for our CNN. These periods will necessarily be significantly shorter than the Fourier period of $2\bar{A}$, and we carefully select the value of $\bar{A}$ for each training data so that the Fourier representation of the edge dislocation period $\bar{A}_{\bar{A}}$ will be approximately in discrete multiples of $\bar{A}$. This approach allows us to superpose the continuum stress field $\bar{A}^{\bar{A}}_{\bar{A}\bar{A}}$ of a significantly reduced set of discrete edge dislocations within the bounds of $-\bar{A} < \bar{A}_1 < \bar{A}$, since the stress fields of the edge dislocations beyond $|\bar{A}_1| \geq \bar{A}$ are implicitly accounted for with the periodic Fourier representation of $\bar{A}^{\bar{A}}_{\bar{A}\bar{A}}$.

We elucidate the improved accuracy of (2) by comparing the compression-neutral-tension stress patterns for this continuum field versus the MD field across the low- to high-tilt-angle grain boundaries in Figs. 7 and 8. We observe a significant improvement in the GBD field representation even for the low- and moderate-tilt-angle boundaries of $\bar{A} = 11.42°$ and 16.26° in Fig. 7 – the features associated with the superposed continuum field are in much better agreement with the MD field compared to the superposed discrete field. Even for the high-tilt-angle boundaries of $\bar{A} = 28.06°$ and 36.86° in Fig. 8, the background noise in the respective superposed atomistic stress field is now completely suppressed for the superposed continuum field due to the enforced equilibrium and symmetry constraints in the spectral treatment, which allows the distinctive tension-compression features associated with the GBDs to re-emerge.

Following the procedure outlined in Section 3, we generate 9,000 samples of the continuum-equivalent stress fields of periodically-spaced edge dislocations for the training, validation, and testing of our CNN, and apply this CNN towards the MD grain boundary models across the range of $\bar{A}$. Our results summarized in Table 1 show that re-training of the CNN based on the continuum stress fields of superposed edge dislocations significantly improves the true negative dislocation detections (by ~13%) while maintaining high true positive dislocation detection accuracies. The mean localization errors are still mostly within one or two pixels from the core, but the localization predictions for $\bar{A} = 36.86°$, which is the highest tilt angle in Table 1, is markedly improved: ~94% of the correctly predicted dislocations now reside within ± 1 Å of the actual GBD, compared to a mere ~2% when the CNN was trained on the discrete dislocation field.

With this improved quality of the training dataset, we show a sampling of the predictions for various sliding detection widows for both $\bar{A} = 28.06°$ and 36.86° in Fig. 9. We now obtain very consistent localization predictions with limited scatter for both boundaries; the average localization

predictions of the CNN (green dislocation symbols) are now very close to the actual dislocation location (cross symbol) at the center of the error bounding box (black). We further push the limits our CNN predictions by examining the localization capabilities when applied to a grain boundary with a very high tilt angle of $\bar{A} = 53.13°$. While we cannot ascertain with high confidence the ground truth location of the GBDs along this particular grain boundary, the scatter in predictions (magenta) across all sliding detection windows is still within reasonable limits, lending confidence to the average predictions (green dislocation symbols) as representative of the grain boundary dislocation structure.

5. Discussions

The multiscale plastic deformation of polycrystalline metals typically initiates from dislocation mechanisms at the grain boundary [55-60]. One of the best approaches for establishing dislocation theories of plasticity is through atomistic and TEM studies on the interaction between dislocations and a single grain boundary [30,61]. However, scaling these dislocation-grain boundary interaction mechanisms to the meso-scale (i.e., polycrystalline grain level) with DDD models has been challenging, because of the lack of an appropriate descriptor of the grain boundary interface. Traditionally, DDD models rely on empirical or phenomenological rules from lower-scale atomistic calculations and experiments to govern the pile-up of dislocations at grain boundaries and the transmission of dislocations through grain boundaries, as well as the dependence of these mechanisms on the orientation and character of the grain boundaries [11-16]. Here, the representation of a grain boundary with GBDs allows for the explicit modeling of unit dislocation-grain boundary interactions in DDD models, and is a critical step towards plasticity modeling of polycrystalline metals across scales.

The notion of GBDs as fundamental elements of a grain boundary structure that create the tilt and twist misorientation adjoining the boundary of two crystalline lattices has been well demonstrated by way of atomistic simulations and transmission electron microscopy (TEM) experiments [19,28,30]. These GBDs in turn generate the atomistic field stresses near the grain boundary, which control fundamental mechanistic processes of dislocation emission, absorption, and pile-up [28-30]. Elucidating the dislocation structure of a boundary from the grain boundary field stresses is therefore an inverse problem, which is particularly challenging for high-tilt-angle grain boundaries due to the overlapping core fields of adjacent GBDs. Our results show that the presence and location of these GBDs across low- to high-tilt-angle grain boundaries can be established with high confidence using CNNs, trained on a dataset generated by superposing the continuum stress fields of unit dislocations. Our predictions capture the transition from sparsely-separated dislocations in low angle grain boundaries, to dislocation clusters with overlapping polymorphic cores in high angle grain boundaries.

Discrete dislocation dynamics (DDD) simulations almost universally ignore core effects, and base the stress field around a dislocation on the analytical linear elastic Volterra solution [11-16]. However, studies have shown that core effects can be significant ~10 to 50Ā (~30 to 150 Å) from the dislocation line [33]. This has motivated the development of analytical solutions for the dislocation core field as cylindrical dilatations caused by a line defect represented by unequal force dipoles, which are in turn superposed on the Volterra field [34]. We have instead obtained a continuum representation of the combined core and Volterra field of an isolated edge dislocation modeled in MD through a spectral method. We find that a CNN, trained on a dataset generated by superposing the continuum fields of randomly-spaced GBDs, is able to accurately quantify the locations of the GBDs even for very high angle grain boundaries with overlapping core fields.

Conversely, we have also trained a CNN based only on the Volterra analytical fields of superposed GBDs, and our results show dramatically reduced true positive detection predictions even for low-tilt-angle grain boundaries, with an inability of the CNN to localize the GBDs (Table S2 of the Supplementary Materials).

Our basic assumption in generating the training dataset is that the principle of superposition holds, and the stress field of the combined grain boundary structure can be well-represented by the superposed stress fields of isolated edge dislocations. This simple assumption appears to be valid for low- to moderate-tilt-angle grain boundaries, where the superposed stress fields of the isolated dislocations closely resemble the actual virial stresses of the grain boundaries from MD simulations (Fig. 5). For high-tilt-angle grain boundaries, however, the superposed stress field increasingly deviates from the actual MD stress field with increasing proximity of the GBDs (Fig. 6c,d), which suggests some levels of core structure changes associated with core-to-core interactions. Nevertheless, the CNN is still able to predict, with high consistency, the location of these closely-spaced GBDs in very high-tilt-angle grain boundaries (Fig. 9). Conceivably, the neural network predictions can be further improved by incorporating the effects of core structural changes (as a function of the tilt angle) into the training dataset. To this end, one possibility is to train the CNN based on the MD stress fields of actual grain boundaries, although this necessitates identifying the dislocation structures of these grain boundaries a priori. We show in Table 2 the ability of CNNs, trained on lower tilt-angle grain boundaries (red entries) to predict the dislocation structures of higher tilt-angle grain boundaries (black entries). Interestingly, the CNN is able to extrapolate its detection of GBDs in high-tilt-angle grain boundaries with high accuracy, but its localization extrapolation capabilities are limited only to the nearest few (at times, one or two) grain boundary models ranked in ascending order of $\bar{A}$. Conversely, training the CNN on very

much fewer grain boundary models, but encompassing grain boundaries over a wider range of $\bar{A}$, allows for excellent interpolative detection and localization capabilities, as shown in Table 3. Even with just three grain boundaries within the training dataset (red entries for CNN-2), the localization predictions on the remaining MD grain boundaries in the testing dataset (black entries) well exceeds 80% within the interpolative range of $\bar{A}$.

While we base our training/testing datasets in this work on dislocation/grain boundary structures modeled with MD simulations, we can similarly train or apply the same neural network architecture to other atomistic models of grain boundaries to predict the corresponding GBD structures, as long as a quantifiable measure of the atomistic stress tensor (stress-per-atom) near the grain boundary exists. In DFT calculations, a numerical technique termed the sequential atom removal (SAR) method was developed to reconstruct the equivalent atomistic (quantum-mechanical) stresses near a grain boundary, in which individual atoms near the boundary were sequentially removed to compute the pair force between atoms, while correcting for changes to the local electron density caused by atom removal [62]. We have reproduced these atomistic stresses from a DFT model of a symmetrical-tilt $\Sigma5(310)[001]$ Cu grain boundary ($\bar{A} = 36.86°$) in Fig. 10a, which are fed as inputs to our CNN trained on the superposed continuum dislocation fields in Section 4.3. We show that this CNN is able to detect the presence of GBDs with true positive and true negative accuracies of 100% and 90%, respectively, along with localization accuracies of 95%. We include in Fig. 10a a sampling of the true positive detection windows, along with the corresponding location of the predicted GBDs from the DFT stress field. Results show that the average GBD location established from the DFT stress field (green dislocation symbol) is within ~0.14 Å of the average location predicted from the MD stress field in Fig. 9b – we superimpose both these GBD predictions (denoted by red and green dislocation symbols, respectively) on a high

resolution TEM image of the same boundary [63] in Fig. 10b. In addition to elucidating the stress state of the grain boundary with atomistic models, experimental techniques have utilized moving dislocations as mechanical probes, digital image correlation, or dark field in-line holography, to achieve sub-nanometer resolution image-based local strain and stress measurements [64-67]. Recent studies have proposed a hybrid MD-TEM approach, using an artificial neural network (ANN) trained on MD data, to quantify the atomistic stresses of a grain boundary from atomic position information provided by TEM imaging [39]. Through our neural network approach, one can conceivably predict the GBD structures from the experimental local stress information of these boundaries.

The present analysis for GBD detection and localization is based on minimum energy symmetrical-tilt <001> grain boundaries, where the GBDs are known to retain their distinctive edge character with Burgers vector oriented perpendicular to the plane of the grain boundary – this significantly simplifies the training dataset. Nevertheless, the study demonstrates for the first time the unique ability of CNNs to predict and localize GBDs in high-tilt-angle grain boundaries, which have eluded well-established approaches based on Burgers circuit analysis [52,53]. Conceivably, the neural network can be extended to also predict the Burgers vectors of GBDs in asymmetrical or metastable grain boundaries [68], localize partial dislocations formed by dissociated GBDs along grain boundaries with different rotation axes (e.g. <110>) [28], or even quantify the mixed screw and edge character of GBDs in 3D microstructures, by incorporating the relevant full/partial and edge/screw dislocation fields within the training dataset. This systematic extension of the CNN towards more realistic microstructures is a subject of future work.

6. Conclusion

We have demonstrated the high accuracy of CNNs in quantifying the edge dislocation structures across a series of <001> symmetrical-tilt Cu grain boundaries. We show that a training dataset generated from the superposed MD stress fields of individual dislocations allows the CNN to predict the GBD structures across a wide range of tilt angles. Training the CNN on continuum representations of the superposed dislocation field, constrained to satisfy equilibrium and symmetry conditions, further improves the localization accuracy, particularly when applied to high-tilt-angle grain boundaries with overlapping core fields. This machine learning approach of detecting the presence and identifying the locations of dislocations with sub-angstrom accuracies is a significant improvement over prior approaches based on Burgers circuit analysis, which is typically limited to low- and moderate-tilt-angle grain boundaries with no overlapping cores. This representation of the atomistic structures of grain boundaries, in terms of unit dislocations as fundamental elements of the boundary, paves the way for the bridging of scales between MD or DFT models of grain boundaries and mesoscale DDD calculations. Such accurate quantification of the dislocation structures of grain boundaries, and hence the local strain distributions, provides rich fundamental insights into the underpinning dislocation mechanics to enable grain boundary engineering.

Acknowledgements

This work is supported by AFOSR Aerospace Materials for Extreme Environment Program under Award No. FA9550-19-1-0242, as well as the National Science Foundation (NSF) under Award Nos. NSF-DMR-18-09696 and NSF-CMMI-2009684. WN acknowledges the support of a DIGI-MAT graduate fellowship based upon work supported by NSF under Grant No. 1922758. We also acknowledge the use of the Advanced Cyberinfrastructure Coordination Ecosystem: Services &

Support (ACCESS) through allocations MAT230069, MAT210031, and MAT230055, and TACC Frontera through allocation MSS22006.

References

[1] J. Kacher, B.P. Eftink, B. Cui, I.M. Robertson, Dislocation interactions with grain boundaries, Curr. Opin. Solid State Mater. Sci. 18 (2014) 227–243.

[2] J. Schiøtz, K.W. Jacobsen, A maximum in the strength of nanocrystalline copper, Science 301 (2003) 1357–1359.

[3] M.A. Meyers, A. Mishra, D.J. Benson, Mechanical properties of nanocrystalline materials, Prog. Mater. Sci. 51 (2006) 427–556.

[4] V. Yamakov, D. Wolf , S.R. Phillpot, A.K. Mukherjee, H. Gleiter, Dislocation processes in the deformation of nanocrystalline aluminum by molecular dynamics simulation, Nat. Mater. 1 (2002) 45–49.

[5] Z. Shan, E.A. Stach, J.M.K. Wiezorek, J.A. Knapp, D.M. Follstaedt, S.X. Mao, Grain boundary-mediated plasticity in nanocrystalline nickel, Science 305 (2004) 654–657.

[6] X. Li, Y. Wei, L. Lu, K. Lu, H. Gao, Dislocation nucleation governed softening and maximum strength in nano-twinned metals, Nature 464 (2010) 877–880.

[7] R. Li, H.B. Chew, Deformation twinning and plastic recovery in Cu/Ag nanolayers under uniaxial tensile straining, Philos. Mag. Lett. 94 (2014) 260–268.

[8] R. Li, H.B. Chew, Planar-to-wavy transition of Cu–Ag nanolayered metals: a precursor mechanism to twinning, Philos. Mag. 95 (2015) 1029–1048.

[9] R. Li , H.B. Chew, Closed and open-ended stacking fault tetrahedra formation along the interfaces of Cu–Al nanolayered metals, Philos. Mag. 95 (2015) 2747–2763.

[10] D.V. Bachurin, D. Weygand, P. Gumbsch, Dislocation–grain boundary interaction in <111> textured thin metal films, Acta Mater 58 (2010) 5232–5241.

[11] M. Huang, S. Huang, S. Liang, Y. Zhu, Z. Li, An efficient 2D discrete dislocation dynamics-XFEM coupling framework and its application to polycrystal plasticity, Int. J. Plast. 127 (2020), 102647.

[12] S.S. Quek, Z. Wu, Y.W. Zhang, D.J. Srolovitz, Polycrystal deformation in a discrete dislocation dynamics framework, Acta Mater. 75 (2014) 92-105.

[13] R. Kumar, F. Székely, E. Van Der Giessen, Modelling dislocation transmission across tilt grain boundaries in 2D, Comput. Mater. Sci. 49 (2010) 46-54.

[14] N. Ahmed, A. Hartmaier, Mechanisms of grain boundary softening and strain-rate sensitivity in deformation of ultrafine-grained metals at high temperatures, Acta Mater. 59 (2011) 4323-4334.

[15] C. Zhou, R. LeSar, Dislocation dynamics simulations of plasticity in polycrystalline thin films, Int. J. Plast. 30-31 (2012) 185-201.

[16] X. Zhang, S. Lu, B. Zhang, X. Tian, Q. Kan, G. Kang, Dislocation–grain boundary interaction-based discrete dislocation dynamics modeling and its application to bicrystals with different misorientations, Acta Mater. 202 (2021) 88-98.

[17] J.W. Cahn, Y. Mishin, A. Suzuki, Duality of dislocation content of grain boundaries, Philos. Mag. 86 (2006) 3965-3980.

[18] D.L. Medlin, S.M. Foiles, D. Cohen, A dislocation-based description of grain boundary dissociation: Application to a 90° <110> tilt boundary in gold, Acta Mater. 49 (2001) 3689-3697.

[19] R.G. Hoagland, S.M. Valone, Emission of dislocations from grain boundaries by grain boundary dissociation, Philos. Mag. 95 (2015) 112-131.

[20] W.T. Read, W. Shockley, Dislocation models of crystal grain boundaries, Phys. Rev. 78 (1950) 275-289.

[21] A.P. Sutton, Grain-boundary structure, Int. Metals Rev. 29 (1984) 377-404.

[22] A.P. Sutton, V. Vitek, On the structure of tilt grain boundaries in cubic metals I. Symmetrical tilt boundaries, Philos. Trans. R. Soc. Lond. A 309 (1983) 1–36.

[23] A.P. Sutton, V. Vitek, On the structure of tilt grain boundaries in cubic metals II. Asymmetrical tilt boundaries, Philos. Trans. R. Soc. Lond. A 309 (1983) 37–54.

[24] A.P. Sutton, V. Vitek, On the structure of tilt grain boundaries in cubic metals. III. Generalizations of the structural study and implications for the properties of grain boundaries, Philos. Trans. R. Soc. Lond. A 309 (1983) 55–68.

[25] G.H. Bishop, B. Chalmers, A coincidence-ledge-dislocation description of grain boundaries, Scr. Metall. 2 (1968) 133–139.

[26] J. Han, V. Vitek, D.J. Srolovitz, The grain-boundary structural unit model redux, Acta Mater. 133 (2017) 186–199.

[27] M.A. Tschopp, D.L. McDowell, Tension-compression asymmetry in homogeneous dislocation nucleation in single crystal copper, Appl. Phys. Lett. 90 (2007) 121916.

[28] R. Li, H.B. Chew, Grain boundary traction signatures: Quantifying the asymmetrical dislocation emission processes under tension and compression, J. Mech. Phys. Solids 103 (2017) 142-154.

[29] R. Li, H.B. Chew, Grain boundary traction signatures: Quantitative predictors of dislocation emission, Phys. Rev. Lett. 117 (2016) 085502.

[30] S. Mohan, R. Li, H.B. Chew, Local stress analysis of partial dislocation interactions with symmetrical-tilt grain boundaries containing E-structural units, Philos. Mag. 98 (2018) 2345-2366.

[31] T.A. Khraishi, J.P. Hirth, H.M. Zbib, T. Diaz de La Rubia, The stress field of a general circular Volterra dislocation loop: Analytical and numerical approaches, Philos. Mag. Lett. 80 (2010) 95-105.

[32] D. Hull, D.J. Bacon, Introduction to Dislocations, fifth ed. Elsevier, 2011.

[33] C.H. Henager Jr., R.G. Hoagland, R.G., Dislocation core fields and forces in FCC metals, Scripta Mater. 50 (2004) 1091-1095.

[34] C.H. Henager Jr., R.G. Hoagland, Dislocation and stacking fault core fields in FCC metals, Philos. Mag. 85 (2005) 4477-4508.

[35] Q. Zhu, A. Samanta, B. Li, R.E. Rudd, T. Frolov, Predicting phase behavior of grain boundaries with evolutionary search and machine learning, Nat. Commun. 9 (2018) 467.

[36] E.R. Homer, D.M. Hensley, C.W. Rosenbrock, A.H. Nguyen, G.L. Hart, Machine-learning informed representations for grain boundary structures, Front. Mater. 6 (2019) 168.

[37] L. Huber, R. Hadian, B. Grabowski, J. Neugebauer, A machine learning approach to model solute grain boundary segregation, Npj Comput. Mater. 4 (2018) 1–8.

[38] S. Zhang, L. Wang, G. Zhu, M. Diehl, A. Maldar, X. Shang, X. Zeng, Predicting grain boundary damage by machine learning. Int. J. Plasticity 150 (2022) 103186.

[39] Y. Cui, H.B. Chew, Machine-learning prediction of atomistic stress along grain boundaries. Acta Mater. 222 (2022) 117387.

[40] F.T. Latypov, E.V. Fomin, V.S. Krasnikov, A.E. Mayer, Dynamic compaction of aluminum with nanopores of varied shape: MD simulations and machine-learning-based approximation of deformation behavior. Int. J. Plasticity 156 (2022) 103363.

[41] D.P. Jang, P. Fazily, J.W. Yoon, Machine learning-based constitutive model for J2-plasticity. Int. J. Plasticity 138 (2021) 102919.

[42] W. Muhammad, A.P. Brahme, O. Ibragimova, J. Kang, K. Inal, A machine learning framework to predict local strain distribution and the evolution of plastic anisotropy and fracture in additively manufactured alloys. Int. J. Plasticity 136 (2021) 102867.

[43] A. Mangal, E.A. Holm, Applied machine learning to predict stress hotspots I: Face centered cubic materials. Int. J. Plasticity 111 (2018) 122-134.

[44] X. Li, C.C. Roth, D. Mohr, Machine-learning based temperature- and rate-dependent plasticity model: Application to analysis of fracture experiments on DP steel. Int. J. Plasticity 118 (2019) 320-344.

[45] J. Chapman, R. Batra, R. Ramprasad, Machine learning models for the prediction of energy, forces, and stresses for Platinum, Comput. Mater. Sci. 174 (2020) 109483.

[46] A.P. Thompson, H.M. Aktulga, R. Berger, D.S. Bolintineanu, W.M. Brown, P.S. Crozier, P.J. in 't Veld, A. Kohlmeyer, S.G. Moore, T.D. Nguyen, R. Shan, M.J. Stevens, J. Tranchida, C. Trott, S.J. Plimpton, LAMMPS – a flexible simulation tool for particle-based materials modeling at the atomic, meso, and continuum scales, Comp. Phys. Comm. 271 (2022) 108171.

[47] S.M. Foiles, M.I. Baskes, M.S. Daw, Embedded-atom-method functions for the fcc metals Cu, Ag, Au, Ni, Pd, Pt, and their alloys, Phys. Rev. B 33 (1986) 7983.

[48] F. Cleri, V. Rosato, Tight-binding potentials for transition metals and alloys, Phys. Rev. B 48 (1993) 22.

[49] N.W. Ashcroft, N.D. Mermin, Solid State Physics, Holt, Rinehart, and Winston, New York, 1976.

[50] G. Simmons, H. Wang, Single Crystal Elastic Constants and Calculated Aggregated Properties: A Hand Book, MIT Press, Cambridge, 1971.

[51] J.P. Hirth, R.C. Pond, R.G. Hoagland, X.-Y. Liu, J. Wang, Interface defects, reference spaces and the Frank–Bilby equation, Prog. Mater. Sci. 58 (2013) 749-823.

[52] A. Stukowski, Visualization and analysis of atomistic simulation data with OVITO–the Open Visualization Tool, Modelling Simul. Mater. Sci. Eng. 18 (2010) 015012.

[53] A. Stukowski, K. Albe, Extracting dislocations and non-dislocation crystal defects from atomistic simulation data, Modelling Simul. Mater. Sci. Eng. 18 (2010) 085001.

[54] L. Alzubaidi, J. Zhang, A.J. Humaidi, A. Al-Dujaili, Y. Duan, O. Al-Shamma, J. Santamaria, M.A. Fadhel, M. Al-Amidie, L. Farhan, Review of deep learning: concepts, CNN architectures, challenges, applications, future directions. J. Big Data 8 (2021) 53.

[55] D.L. McDowell, A perspective on trends in multiscale plasticity, Int. J. Plasticity 26 (2010) 1280-1309.

[56] G.J. Tucker, D.L. McDowell, Non-equilibrium grain boundary structure and inelastic deformation using atomistic simulations, Int. J. Plasticity 27 (2011) 841-857.

[57] G.J. Tucker, S.M. Foiles, Quantifying the influence of twin boundaries on the deformation of nanocrystalline copper using atomistic simulations, Int. J. Plasticity 65 (2015) 191-205.

[58] Q. Huang, Q. Zhao, H. Zhou, W. Yang, Misorientation-dependent transition between grain boundary migration and sliding in FCC metals, Int. J. Plasticity 159 (2022) 103466.

[59] E.N. Borodin, A.E. Mayer, M. Yu Gutkin, Coupled model for grain rotation, dislocation plasticity and grain boundary sliding in fine-grained solids, Int. J. Plasticity 134 (2020) 102776.

[60] H. Lim, M.G. Lee, J.H. Kim, B.L. Adams, R.H. Wagoner, Simulation of polycrystal deformation with grain and grain boundary effects, Int. J. Plasticity 27 (2011) 1328-1354.

[61] M.D. Sangid, H.J. Maier, H. Sehitoglu, The role of grain boundaries on fatigue crack initiation – An energy approach, Int. J. Plasticity 27 (2011) 801-821.

[62] Y. Cui, H.B. Chew, A simple numerical approach for reconstructing the atomic stresses at grain boundaries from quantum-mechanical calculations, J. Chem. Phys. 150 (2019) 144702.

[63] G. Duscher, M. Chisholm, U. Alber, M. Rühle, Bismuth-induced embrittlement of copper grain boundaries, Nature Mater. 3 (2004) 621-626.

[64] C.T. Koch, V.B. Özdöl, P.A. Van Aken, An efficient, simple, and precise way to map strain with nanometer resolution in semiconductor devices, Appl. Phys. Lett. 96 (2010) 091901.

[65] M. Hÿtch, F. Houdellier, F. Hüe, E. Snoeck, Nanoscale holographic interferometry for strain measurements in electronic devices, Nature 453 (2008) 1086–1089.

[66] A. Béché, J.L. Rouvière, J.P. Barnes, D. Cooper, Strain measurement at the nanoscale: Comparison between convergent beam electron diffraction, nano-beam electron diffraction, high resolution imaging and dark field electron holography, Ultramicroscopy 131 (2013) 10–23.

[67] M. Legros, In situ mechanical TEM: Seeing and measuring under stress with electrons, Comptes Rendus Phys. 15 (2014) 224–240.

[68] J. Han, V. Vitek, D.J. Srolovitz, Grain-boundary metastability and its statistical properties, Acta Mater. 104 (2016) 259-273.

Table 1: Detection and localization testing accuracies across grain boundaries with various tilt-angles ($\bar{A}$) of a CNN trained on (a) superposed discrete dislocation stress field and (b) superposed continuum dislocation stress field.

$\bar{A}$ (°)	$\bar{A}_{\bar{A}}$ (Å)	**Train: Discrete Dislocation Stress Field**					**Train: Continuum Dislocation Stress Field**				
		Detect (%)		*Localize*			*Detect (%)*		*Localize*		
		True positive	True negative	±1 Å Box (%)	$\Delta\bar{A}_1$ (Å)	$\Delta\bar{A}_2$ (Å)	True positive	True negative	±1 Å Box (%)	$\Delta\bar{A}_1$ (Å)	$\Delta\bar{A}_2$ (Å)
3.28	63.3	100	81	95	-0.24	0.32	100	99	100	0.26	-0.11
3.95	52.4	100	82	95	-0.24	0.33	100	99	100	0.26	-0.11
4.24	48.8	100	81	95	-0.24	0.33	100	99	100	0.26	-0.10
5.45	38.0	100	81	86	-0.02	-0.14	99	99	81	0.12	-0.16
5.73	36.2	100	82	85	-0.06	-0.08	97	99	83	0.14	-0.05
6.73	30.8	100	84	85	-0.05	-0.21	99	98	86	0.14	-0.06
8.17	25.4	100	83	86	-0.02	-0.13	98	98	85	0.14	-0.05
8.80	23.6	100	83	90	0.03	-0.09	100	98	85	0.07	-0.10
10.39	20.0	100	82	90	0.03	-0.10	95	99	86	0.19	-0.14
11.42	18.2	100	83	90	0.09	-0.02	96	99	84	0.16	-0.10
12.68	16.4	100	84	91	0.14	0.03	96	99	86	0.10	-0.02
14.25	14.6	100	85	96	0.20	0.01	92	99	85	0.21	-0.12
16.26	12.8	100	86	94	0.23	0.01	84	99	81	0.18	-0.20
18.93	11.0	100	89	89	0.08	0.22	87	99	80	0.10	-0.01
22.62	9.2	100	91	89	0.24	0.22	95	98	80	0.20	-0.01
28.06	7.5	100	93	93	-0.27	-0.14	100	97	95	0.34	0.08
36.86	5.7	100	97	2	-2.01	-1.30	100	97	94	-0.04	-0.21
Average		100	85	85	-0.12	0.25	96	98	88	0.17	-0.09

Table 2: Extrapolative capabilities of a CNN trained on the stress field of actual MD grain boundaries: Detection and localization training and testing accuracies across grain boundaries with various tilt-angles (Ā). Red, bold: training dataset. Black: testing dataset.

Ā (°)	CNN-1			CNN-2			CNN-3			CNN-4		
	Detect and Localize (%)			*Detect and Localize (%)*			*Detect and Localize (%)*			*Detect and Localize (%)*		
	True positive	True negative	±1 Å Box	True positive	True negative	±1 Å Box	True positive	True negative	±1 Å Box	True positive	True negative	±1 Å Box
3.28	**100**	**100**	**95**	**100**	**100**	**88**	**100**	**100**	**95**	**100**	**100**	**100**
3.95	**100**	**100**	**95**	**100**	**100**	**89**	**100**	**100**	**95**	**100**	**100**	**100**
4.24	**100**	**100**	**95**	**100**	**100**	**90**	**100**	**100**	**95**	**100**	**100**	**100**
5.45	**99**	**100**	**97**	**100**	**100**	**91**	**100**	**100**	**96**	**100**	**100**	**99**
5.73	**99**	**100**	**93**	**100**	**100**	**90**	**100**	**100**	**96**	**100**	**100**	**98**
6.73	100	100	96	**100**	**100**	**94**	**100**	**100**	**97**	**100**	**100**	**100**
8.17	100	100	94	**99**	**100**	**92**	**100**	**100**	**96**	**100**	**100**	**99**
8.80	94	100	94	**97**	**100**	**95**	**100**	**100**	**100**	**99**	**100**	**100**
10.39	93	100	87	96	100	92	**99**	**100**	**99**	**99**	**100**	**99**
11.42	99	100	90	95	100	89	**100**	**100**	**98**	**100**	**100**	**99**
12.68	99	100	88	93	100	86	**100**	**100**	**96**	**100**	**100**	**100**
14.25	93	99	79	96	100	79	91	99	95	**100**	**100**	**99**
16.26	89	99	47	88	100	66	81	99	75	**96**	**100**	**99**
18.93	93	100	32	74	100	67	83	100	52	**100**	**100**	**100**
22.62	96	100	17	74	100	49	78	100	33	**100**	**100**	**99**
28.06	94	98	13	78	100	46	82	99	3	95	99	87
36.86	97	99	21	71	100	20	79	100	1	97	100	10

Table 3: Interpolative capabilities of a CNN trained on the stress field of actual MD grain boundaries: Detection and localization training and testing accuracies across grain boundaries with various tilt-angles (Ā). Red, bold: training dataset. Black: testing dataset.

Ā (°)	CNN-1			CNN-2			CNN-3		
	Detect and Localize (%)			*Detect and Localize (%)*			*Detect and Localize (%)*		
	True positive	True negative	±1 Å Box	True positive	True negative	±1 Å Box	True positive	True negative	±1 Å Box
3.28	**100**	**100**	**94**	**100**	**100**	**94**	**100**	**100**	**95**
3.95	100	100	94	100	100	95	100	100	96
4.24	100	100	94	100	100	95	100	100	96
5.45	85	100	57	92	100	91	100	100	95
5.73	84	100	55	89	100	91	**100**	**100**	**95**
6.73	88	100	60	93	100	93	100	100	93
8.17	88	100	65	94	100	93	97	100	95
8.80	84	100	68	**100**	**100**	**94**	100	100	95
10.39	85	100	74	99	100	92	**99**	**100**	**99**
11.42	88	100	75	94	100	94	95	100	98
12.68	91	100	80	94	100	94	95	100	96
14.25	88	100	76	98	100	90	**100**	**100**	**99**
16.26	94	97	65	94	97	84	96	100	93
18.93	100	99	80	99	99	85	95	100	91
22.62	**100**	**100**	**100**	**100**	**100**	**100**	**100**	**100**	**100**
28.06	95	99	97	95	99	88	95	99	91
36.86	95	100	6	89	100	10	94	100	23

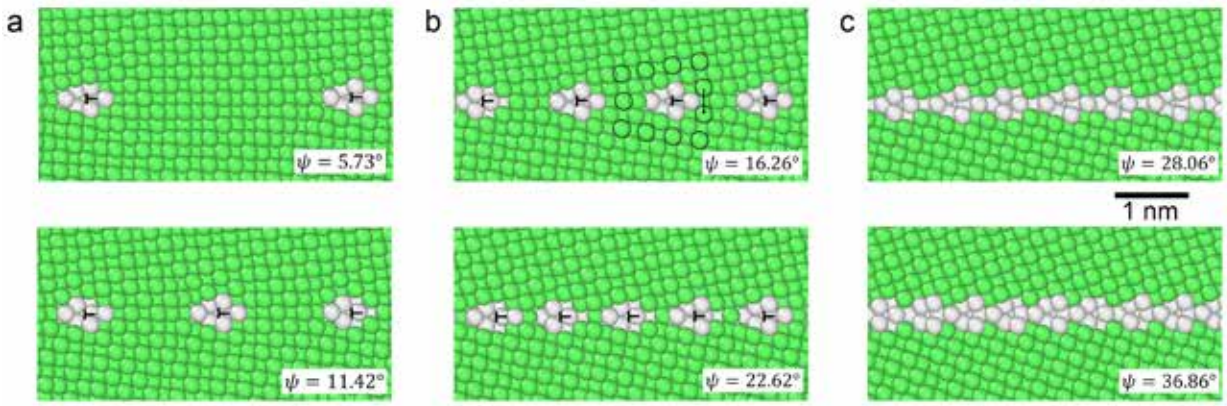

Fig. 1: Atomistic configurations of low- (**a**), moderate- (**b**), and high-tilt-angle (**c**) <001> Cu grain boundaries constructed by MD simulations. Atoms are colored according to the common neighbor analysis: green – FCC, white – other coordination structure. Outlined atoms in (**b-top**) depict example of a Burgers circuit. Dislocation symbols in (**a**) and (**b**) denote predicted dislocation locations from DXA analysis.

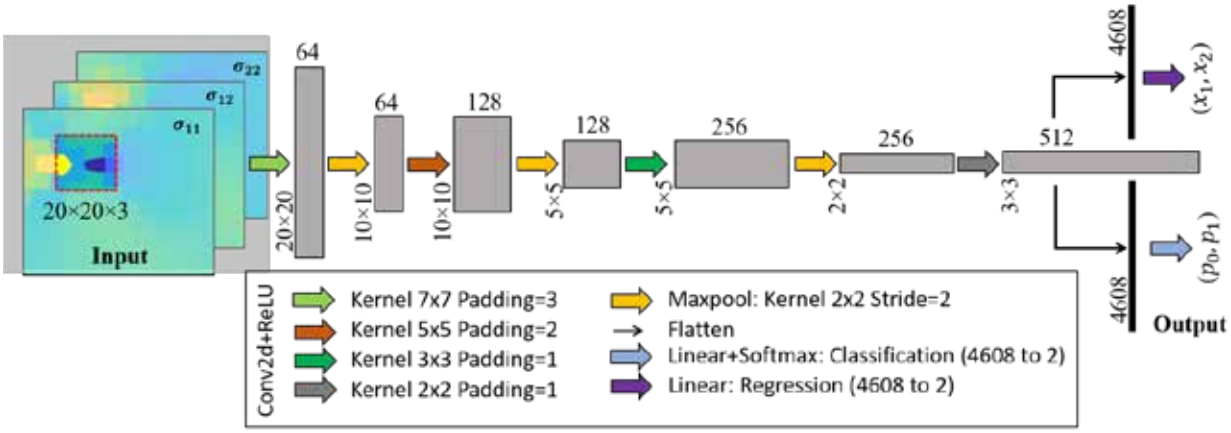

Fig. 2: Architecture of a convolutional neural network (CNN) to detect the presence or absence of dislocations with probability $\bar{A}_0$ or $\bar{A}_1 = 1 - \bar{A}_0$ and predict its corresponding $(\bar{A}_1, \bar{A}_2)$ location, from the atomistic $(\bar{A}_{11}, \bar{A}_{12}, \bar{A}_{22})$ stress images within the sliding detection window (red outline).

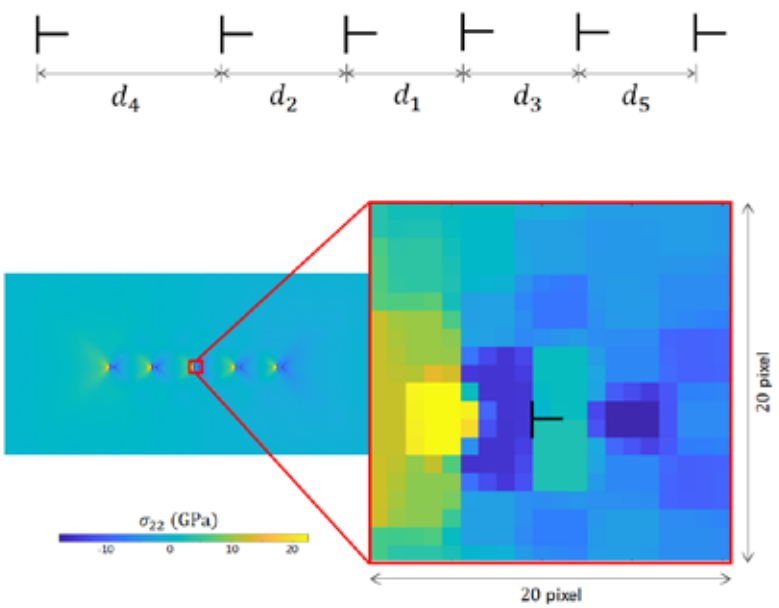

Fig. 3: Training of a CNN with pseudo GBD structures. Top: instantiation of randomly-spaced edge dislocations along a grain boundary. Bottom: pseudo grain boundary stress field from superposing the discrete stress fields of isolated edge dislocations from MD simulations.

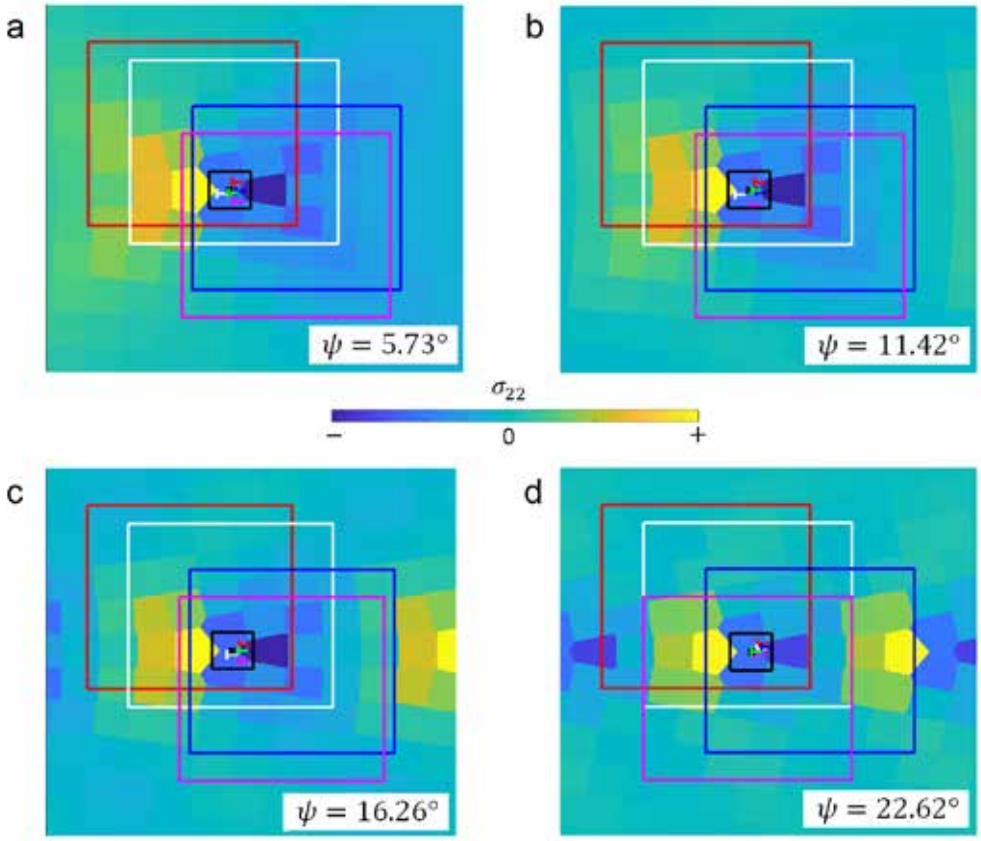

Fig. 4: Sampling of detection windows (colored boxes) where true positive edge dislocations are detected for low- (**a,b**) and moderate-tilt-angle (**c,d**) grain boundaries, along with the predicted dislocation locations (corresponding colored dislocation symbols). Green dislocation symbol: average predicted dislocation location across all positive detection windows. Black box: ±2 pixel error bound centered about the actual dislocation location (black cross).

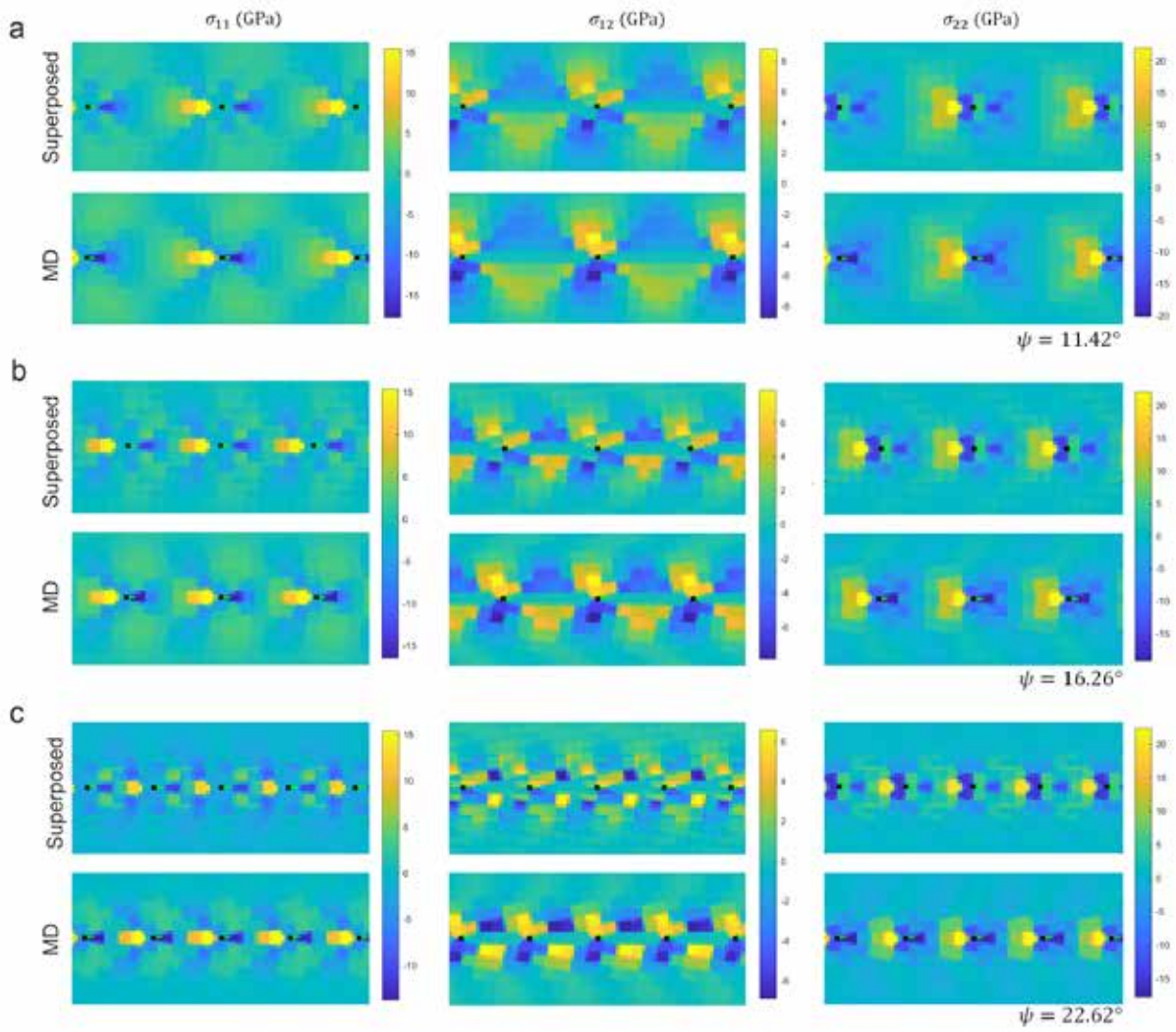

Fig. 5: Comparison of the superposed stress fields of isolated dislocations versus the actual grain boundary stress fields from MD simulations for low- and moderate-tilt-angle grain boundaries. Green dislocation symbol: predicted dislocation location. Black cross: actual dislocation location.

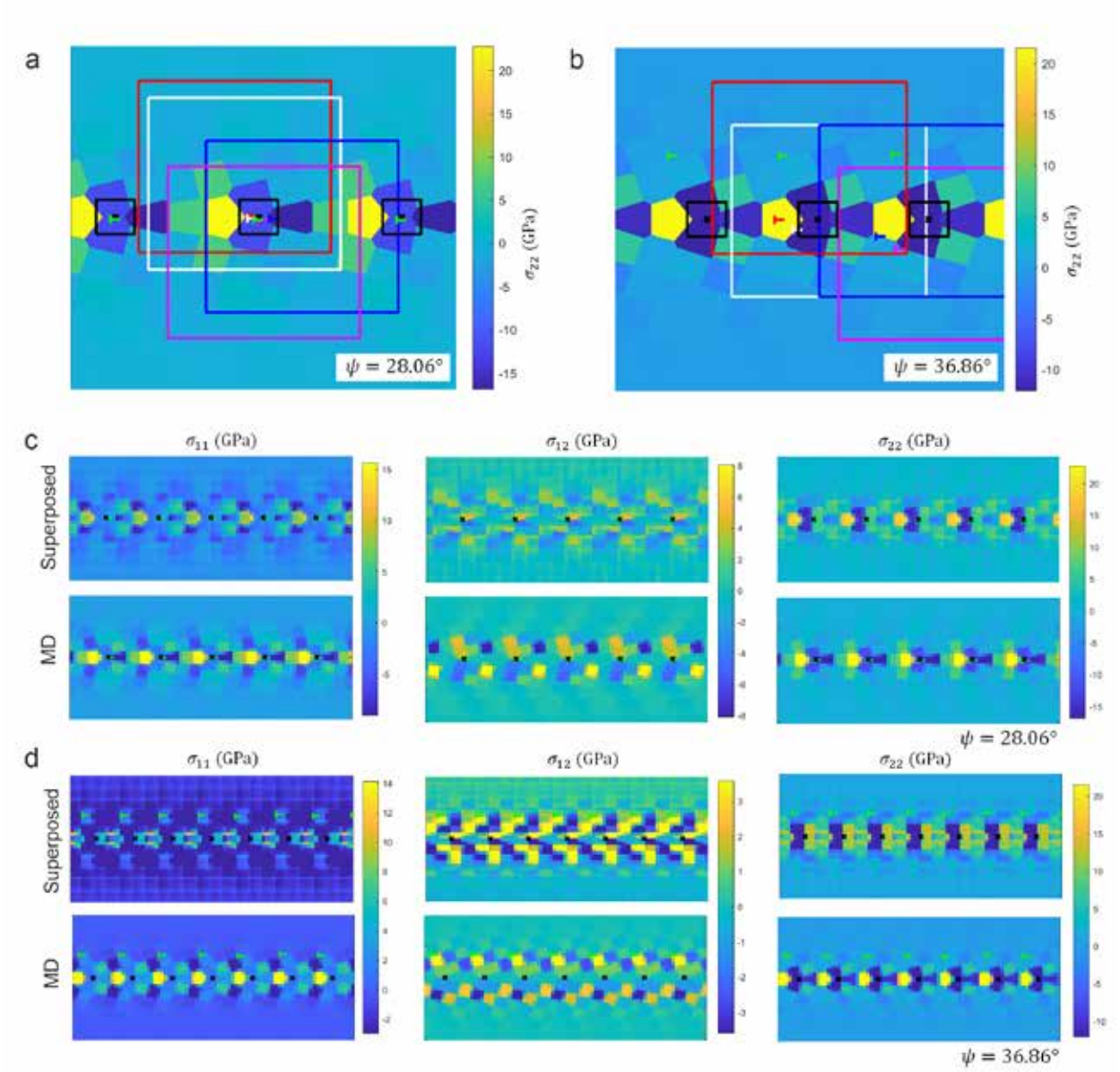

Fig. 6: High-tilt-angle grain boundaries: (**a,b**) Sampling of detection windows (colored boxes) where true positive edge dislocations are detected, along with the predicted dislocation locations (corresponding colored dislocation symbols). Green dislocation symbol: average predicted dislocation location across all positive detection windows; black box: ±2 pixel error bound centered about the actual dislocation location (black cross). (**c,d**) Comparison of the superposed stress fields of isolated dislocations versus the actual grain boundary stress fields from MD simulations.

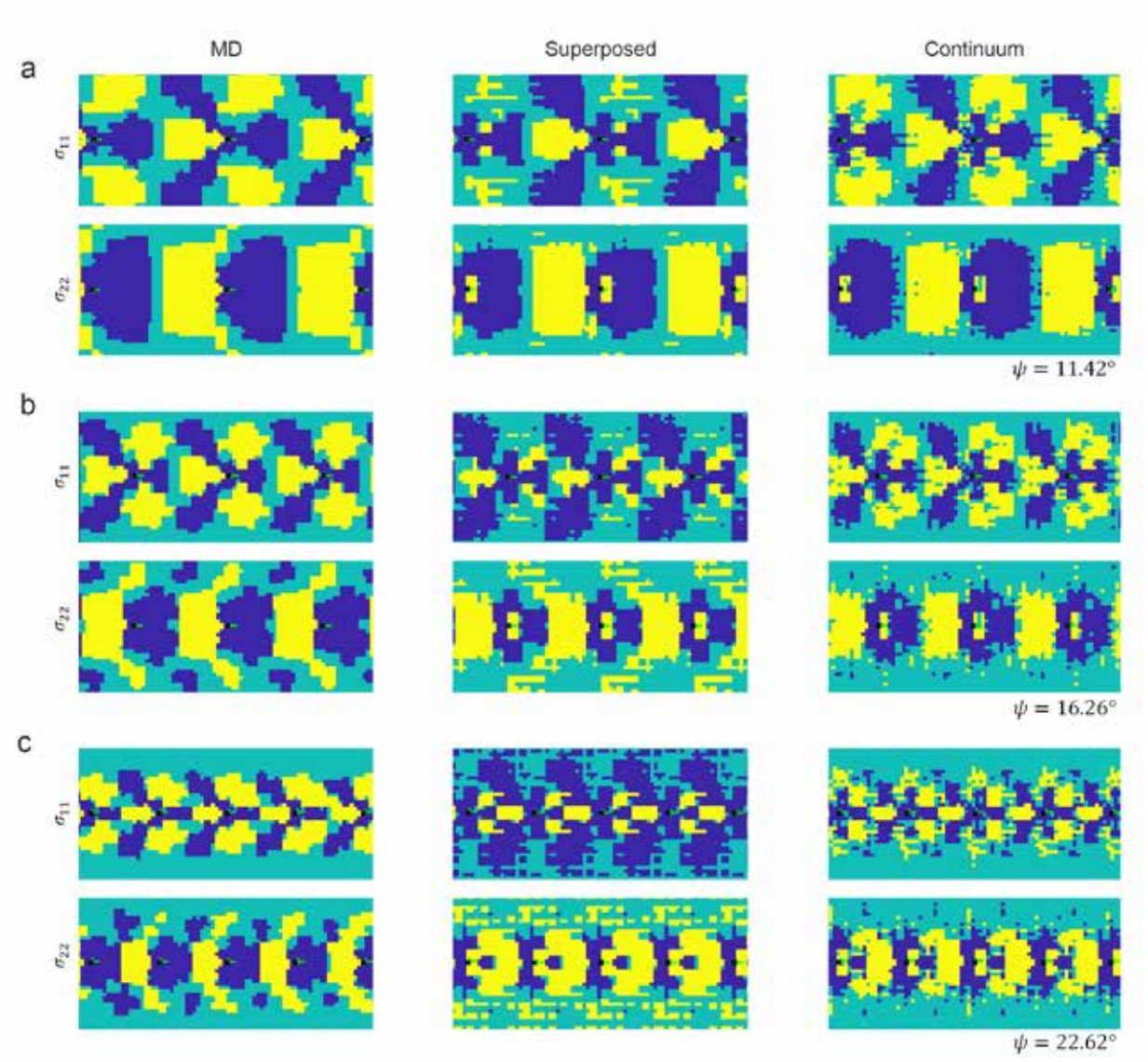

Fig. 7: Tension and compression contours of the grain boundary stress fields from MD versus the superposed discrete and continuum stress fields of isolated dislocations for low- and moderate-tilt-angle grain boundaries. Yellow: $\bar{A}_{\bar{A}\bar{A}} > 1$ GPa; blue: $\bar{A}_{\bar{A}\bar{A}} < -1$ GPa; pale green: $\left|\bar{A}_{\bar{A}\bar{A}}\right| \leq 1$ GPa.

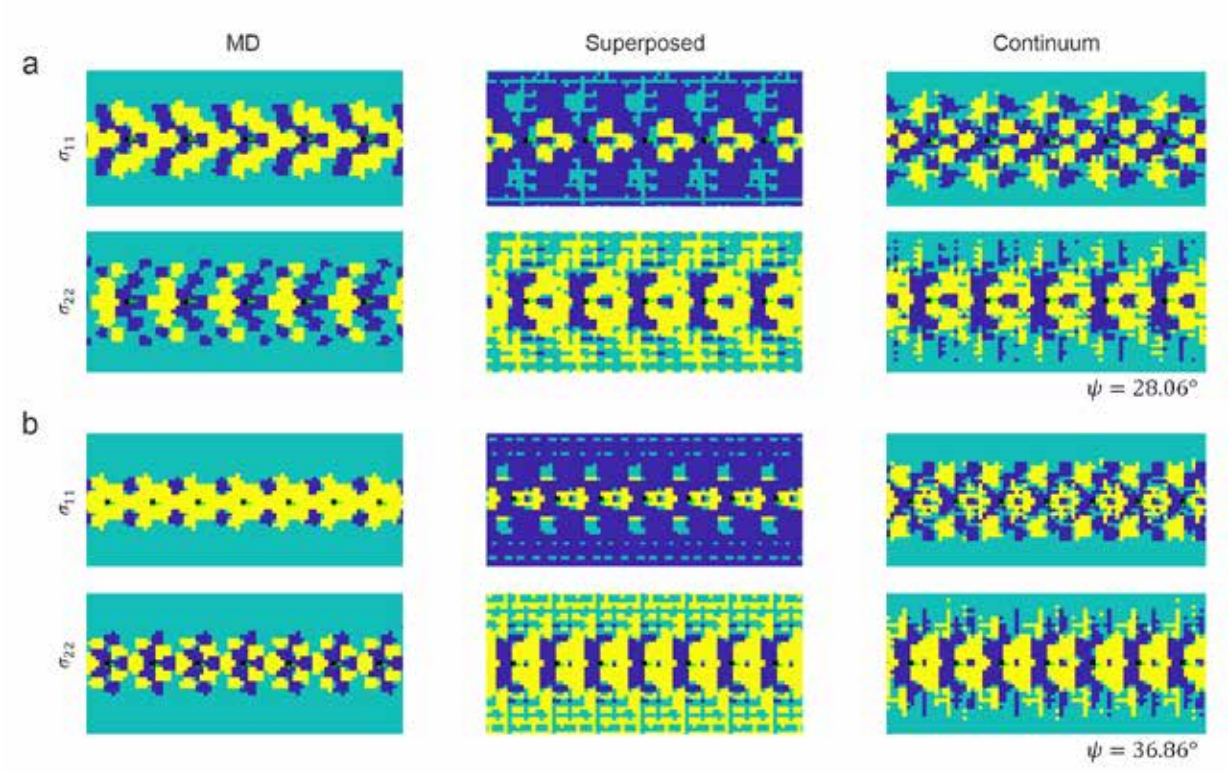

Fig. 8: Tension and compression contours of the grain boundary stress fields from MD versus the superposed discrete and continuum stress fields of isolated dislocations for high-tilt-angle grain boundaries. Yellow: $\bar{A}_{\bar{A}\bar{A}} > 1$ GPa; blue: $\bar{A}_{\bar{A}\bar{A}} < -1$ GPa; pale green: $\left|\bar{A}_{\bar{A}\bar{A}}\right| \leq 1$ GPa.

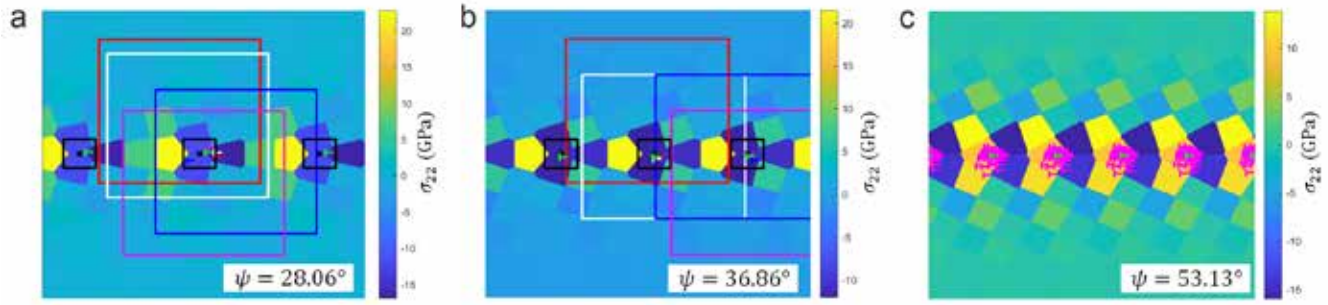

Fig. 9: Dislocation structures of high-tilt-angle grain boundaries from CNN trained on the superposed continuum stress fields of isolated dislocations. Colored boxes and dislocation symbols: sampling of detection windows for true positive edge dislocation with corresponding dislocation locations; black box: ±2 pixel error bound centered about the actual dislocation location (black cross); green dislocation symbol: average predicted dislocation location across all positive detection windows.

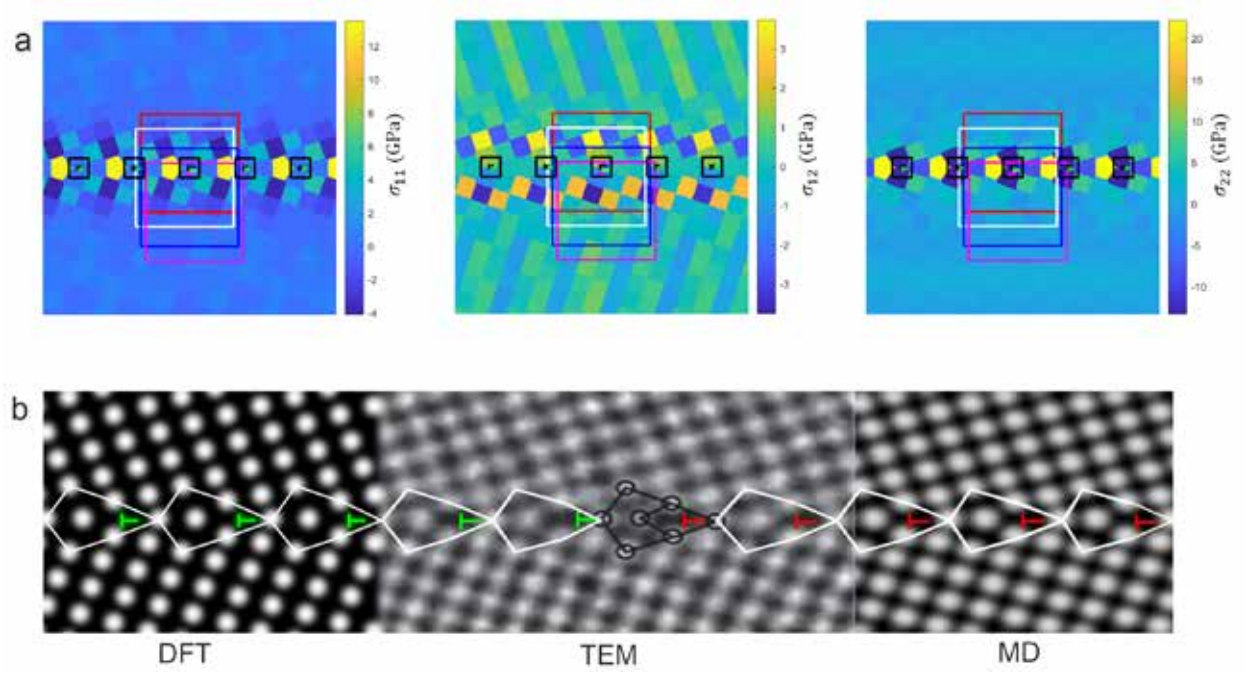

Fig. 10: DFT computations of GBDs for high-tilt-angle grain boundary with $\bar{A} = 36.86°$. (**a**) Stress-per-atom computations, with colored boxes and dislocation symbols denoting sampling of detection windows for true positive edge dislocations with corresponding dislocation locations; black box: ±2 pixel error bound centered about the actual dislocation location (black cross). (**b**) Comparison of DFT, TEM, and MD grain boundary structures; green and red dislocation symbols: average predicted dislocation location from DFT- and MD-generated grain boundaries across all positive detection windows.